






Article

The Role of Aerosol Concentration on Precipitation in a Winter Extreme Mixed-Phase System: The Case of Storm Filomena

Enrique Pravia-Sarabia ¹, Juan Pedro Montávez ^{1,*}, Amar Halifa-Marin ¹, Pedro Jiménez-Guerrero ¹
and Juan José Gomez-Navarro ²

¹ Physics of the Earth, Regional Campus of International Excellence (CEIR) “Campus Mare Nostrum”, University of Murcia, 30100 Murcia, Spain

² Agencia Estatal de Meteorología, 28040 Madrid, Spain

* Correspondence: montavez@um.es

Abstract: Aerosol concentration, size and composition are fundamental in hydrometeor formation processes. Meteorological models often use prescribed aerosol concentrations and a single substance. In this study, we analyze the role of aerosol concentration, acting both as CCN and IN, in the development of precipitation in a mixed phase system in numerical weather simulations. To this end, Storm Filomena was selected as the case study. In such a mixed-phase system, the coexistence of supercooled water with ice crystals, as well as the particular existence of a thermal inversion, led to the formation of precipitation in the form of rain, snow and graupel. Several high resolution experiments varying the fixed background aerosol concentration as well as a simulation with an interactive aerosol calculation were performed by means of the WRF-Chem model, using the same physics suite, domain and driving conditions. Results show that the total precipitation remains basically unaltered, with maximum changes of 5%; however, the production of snow is heavily modified. The simulation with maximum prescribed aerosol concentration produced 27% more snow than the interactive aerosol simulation, and diminished the graupel (74%) and rain production (28%). This redistribution of precipitation is mainly linked to the fact that under fixed ice crystal population the variation of aerosol concentration translates into changes in the liquid water content and droplet size and number concentration, thus altering the efficiency of precipitation production. In addition, while modifying the prescribed aerosol concentration produces the same precipitation pattern with the concentration modulating the precipitation amount, interactive aerosol calculation leads to a different precipitation pattern due to the spatial and temporal variability induced in the dynamical aerosol distribution.

Keywords: aerosols; precipitation; WRF; microphysics; mixed phase; regional models



Citation: Pravia-Sarabia, E.; Montávez, J.P.; Halifa-Marin, A.; Jiménez-Guerrero, P.; Gomez-Navarro, J.J. The Role of Aerosol Concentration on Precipitation in a Winter Extreme Mixed-Phase System: The Case of Storm Filomena. *Remote Sens.* **2023**, *15*, 1398. <https://doi.org/10.3390/rs15051398>

Academic Editor: Alexander Kokhanovsky

Received: 4 January 2023

Revised: 15 February 2023

Accepted: 23 February 2023

Published: 1 March 2023



Copyright: © 2023 by the authors. Licensee MDPI, Basel, Switzerland. This article is an open access article distributed under the terms and conditions of the Creative Commons Attribution (CC BY) license (<https://creativecommons.org/licenses/by/4.0/>).

1. Introduction

Mixed-phase clouds constitute a three-phase colloidal system consisting of water vapor, ice particles, and coexisting supercooled liquid droplets [1]. Due to the widespread nature of these systems, whose presence extends from polar to tropical latitudes, their processes and interactions have a direct impact at both a regional and a global scale. Specifically, the interactions of hydrometeors in the three phases, along with temperature and dynamic factors, determine the evolution of precipitation formation. Since the 1950s, numerous studies have examined the development of precipitation in warm clouds, where the condensational or hygroscopic growth plays a key role in the initial stage, and the collision–coalescence (C–C) processes govern the intermediate and mid stages of precipitation formation (see, e.g., [2,3]). In this type of system, the presence of cloud condensation nuclei (CCN) has paramount importance for cloud formation, and the nature of aerosols, namely their hygroscopicity and size, shapes the efficiency of precipitation production. However, the development of precipitation formation processes in mixed-phase clouds is

less known due to the complex interactions that govern them. In spite of many decades of observations and theoretical studies, our knowledge and understanding of mixed-phase cloud processes remain incomplete. Indeed, mixed-phase clouds are difficult to represent in numerical weather prediction and climate models, and their description in theoretical cloud physics still presents a challenge [1].

By the early twentieth century, the original work by Wegener [4] pointed out that, in coexistence of ice crystals and supercooled liquid droplets, the former grow at the expense of the evaporation of the latter provided that the equilibrium water vapor pressure is lower over ice crystals than over liquid droplets. On the basis of the previous work of Wegener, Bergeron (1935) described an ice crystal precipitation theory suggesting that the number concentration of ice particles in mixed-phase clouds must be much smaller than that of cloud droplets, given that only in this case could ice particles grow to precipitable sizes [5]. Findeisen [6] then contributed to this theory with the experimental confirmation of enhanced growth of ice in the mixed phase, providing both theoretical calculations and in situ observations. The theory of ice crystal growth to form precipitation is usually referred to as the Wegener–Bergeron–Findeisen (WBF) process and constitutes one of the fundamentals of cloud physics. Later works on mixed-clouds have focused on the complex task of understanding the interactions between the three phases involved in these systems. Although it is well-known that changes in aerosol number concentration induce variations in the liquid water content (LWC) and the concentration and size of cloud droplets [7,8], the response of ice- and mixed-phase clouds to such changes is not as well defined. In this regard, the role of aerosols in the evolution of mixed-phase clouds is the subject of ongoing studies.

According to early observations of Bigg [9], freezing nuclei may be important at temperatures above about -20°C , while their presence at lower temperatures could be masked by the freezing of uncontaminated drops. Recent works state that ice nucleation in the troposphere via homogeneous freezing occurs at temperatures lower than -38°C and relative humidity with respect to ice above 140% [10]. Thus, ice nuclei activation through immersion and contact freezing remain as the main source of incipient ice crystals. With respect to their growth, ice crystals grow by vapor deposition and riming, i.e., accretion and freezing of supercooled drops [11]. Several authors (see, e.g., [12]) have concluded that the WBF process is important in the dissipative stage of convective clouds, where lower supersaturations are found, and the supply of water vapor for deposition at the expense of evaporation of cloud droplets is expected to be primary. In our case study, updrafts are not strong since the system is not vertically developed, and thus the WBF mechanism should mediate in all stages; indeed, the WBF process is expected to represent the principal means of ice crystal growth for temperatures between -8 and -18°C , where it presents its maximum efficiency.

The efficiency of this process depends on the number of IN (ice nuclei) and CCN. An increase in the ratio of CCN to IN enhances the evaporation and deposition ratios, i.e., the efficiency of WBF [13]. The WBF mechanism should be accompanied by the ice riming process, whose efficiency, according to numerous studies, responds to increased CCN conditions in different ways depending on the case and models [14]. Some authors (see, e.g., [15]) point to a decrease in the riming efficiency under polluted conditions. Others suggest that small droplets formed under higher CCN concentration are more easily transferred to the layers above the freezing level. This would increase the concentration of supercooled cloud droplets and promote the ice-phase microphysical processes, such as riming and the WBF process [16]. Theoretically, the decreased droplet size due to increased CCN is expected to increase the presence of supercooled water in high atmospheric levels by the lifetime effect, thus enhancing the ice riming efficiency. However, as occurs with the C–C processes in warm phase systems, increased droplet sizes enhance warm rain initiation due to the larger probability of collision with bigger droplets. Therefore, a trade-off should exist between these two effects that could be the origin of the case dependence for the ice riming efficiency under increased aerosol conditions.

Furthermore, the ice splintering or secondary ice production [17] could have a relatively high impact on the microphysics of a mixed-phase system. Specifically, increases in CCN increase the cloud droplet number concentration and decrease supercooled liquid droplet size, thus inhibiting ice crystal formation through less efficient secondary ice crystal production [1]. Not implemented in the microphysics of the model employed for this work, secondary ice production is an important factor that should be taken into account in order to properly reproduce the microphysics evolution of a mixed-phase system. Moreover, graupel formation is prone to appear. Early works [18] suggested that graupel is formed by the accretion and freezing of cloud droplets on parent ice particles. Scott and Hobbs [19] introduced the dependence of the formed graupel on the relative size of ice crystals and supercooled droplets, pointing out that freezing droplets due to collisions between small ice crystals and larger cloud drops were the primary sources of graupel embryos. According to the later theory of Matsuo et al. [20], for LWC above $0.4 \text{ g} \cdot \text{m}^{-3}$ and droplets larger than $10 \text{ }\mu\text{m}$ in radius, the formation of graupel is favourable instead of ice crystal growth when contact freezing takes place; in addition, early works pointed out that graupel grows in the updraft regions of cumulus clouds [2], an hypothesis also supported by more recent literature [21,22]; in our case, the frontal surface is expected to be the zone with the most intense updrafts. Hence, it is expected that overall, the increase in CCN concentrations inhibits rain and graupel production and enhances snowfall.

As introduced by Thériault and Stewart [23], there exists a transition in the precipitation type along a winter warm front, ranging from rain behind the front to snow ahead of it, and showing freezing rain and ice pellets just below the warm front, where a thermal inversion is present in the vertical direction, and phase transitions exist. Indeed, Storm Filomena was configured as a feeder-seeder system in which the supercooled water above the frontal surface may be collected by the ice crystals falling from higher altitudes, a configuration expected to enhance precipitation [24]. Therefore, it is foreseeable that the increase in LWC due to a large CCN will reinforce precipitation in this meteorological condition.

In summary, according to the literature, concentrations of cloud condensation nuclei (CCN) and ice nuclei (IN), as well as their activation mechanisms, largely affect the partitioning of condensed water in mixed-phase clouds [25]. Even though there is a general understanding of how aerosols may affect mixed-phase clouds, more dedicated studies in this direction are required. The particular purpose of this research is to investigate the potential benefits of simulating the precipitation of a winter storm with an interactive aerosols approach. Partially approached by [26] for the case of orographic precipitation in the Colorado Rockies, the authors concluded that spatial and temporal variations in CCN predicted by the emissions scheme produced a complicated response in the surface distribution of precipitation from the orographic snowstorm, a result not seen in studies where CCN concentrations are set to be horizontally homogeneous (see, e.g., [27,28]). Thus, this problem remains unsolved, and in the particular case study addressed herein may shed light on the modification of the microphysical processes in a mixed-phase system by part of aerosols and determine whether their interactive calculation is a requirement for a correct modeling of extreme snowfall events. In pursuit of this objective, this paper is organized as follows: first, the meteorological situation of the Filomena storm is described, and the model configuration is described. Then, the results concerning the sensitivity of the model to the constant aerosol concentration and the effect of introducing a dynamic modeling of aerosols are presented.

2. Methodology

2.1. Storm Filomena

During the last days of December 2020 and the first days of January 2021, an intense flux of air from polar latitudes maintained the presence of a cold air mass over Western Europe, which dramatically reduced the temperature to below zero on practically the entire Iberian Peninsula. Moreover, the positioning of a high pressure system in the North Atlantic forced cyclones to follow tracks going much further south. The instability associated with these lows primarily affected the western Canary Islands owing to the arrival of successive Atlantic fronts. In addition, some of these lows were strong enough to reach the Iberian Peninsula with intense activity, as was the case of Filomena [29].

Engendered in the interior of the Eastern USA between 1 and 2 January 2021, Filomena moved northeastward while fully acquiring the characteristics of an extratropical low. On 3 January, the storm entered oceanic locations through Nova Scotia, Canada, from where it was carried away by a southern lobe of the Polar Jet Stream from that day to the following. As it moved eastward over the Atlantic, it lost part of its extratropical structure and weakened; it was not until the next day, when Filomena was positioned with its center close to the Azores Islands, that the official meteorological agency of Spain named it due to the warnings associated with its influence over the Canary Islands between 6 and 7 January, and over the Iberian Peninsula from 7 January onwards. Meanwhile, 6 January, a cold front had released intense winds and precipitation across the Canary Islands, as did Filomena late that day and the following one. Within 48 h of Filomena's arrival in the Canary Islands, it partially acquired tropical characteristics and strengthened as it encountered warmer ocean temperatures.

Throughout 8 January, the storm, again showing an extratropical structure (with cold, warm and occluded fronts), rapidly displaced in a northeasterly direction (see Figure 1). On its arrival at the southernmost border of the Iberian Peninsula (IP), the moist and warm air of Filomena flowed over the much colder air that had settled over the peninsula for weeks, producing strong snowfalls at unusually low altitudes in the center and northeast quadrant during 8 and 9 January. The snow level varied significantly with a marked north–south gradient, leading to snow levels as high as 1200 m in southern Spain in contrast to the low level of 200 m in the mid and northern Iberian Peninsula. Undeniably, the most remarkable effect of Storm Filomena over Spain was the extraordinarily heavy snowfall in extensive areas of the center and eastern peninsular inland regions, where more than 50 cm of snow depth was registered. Other associated effects, such as the flash floods registered in western Spain and Portugal or the intense wind gusts produced at coastal locations, originated from the direct influence of Filomena. After the fading of Filomena and due to the clear skies that followed in the days after 10 January, in combination with the snow cover produced by Filomena, a meteorological cold snap began and extended from 11 to 17 January, with generalized frosts and record-breaking low temperatures.

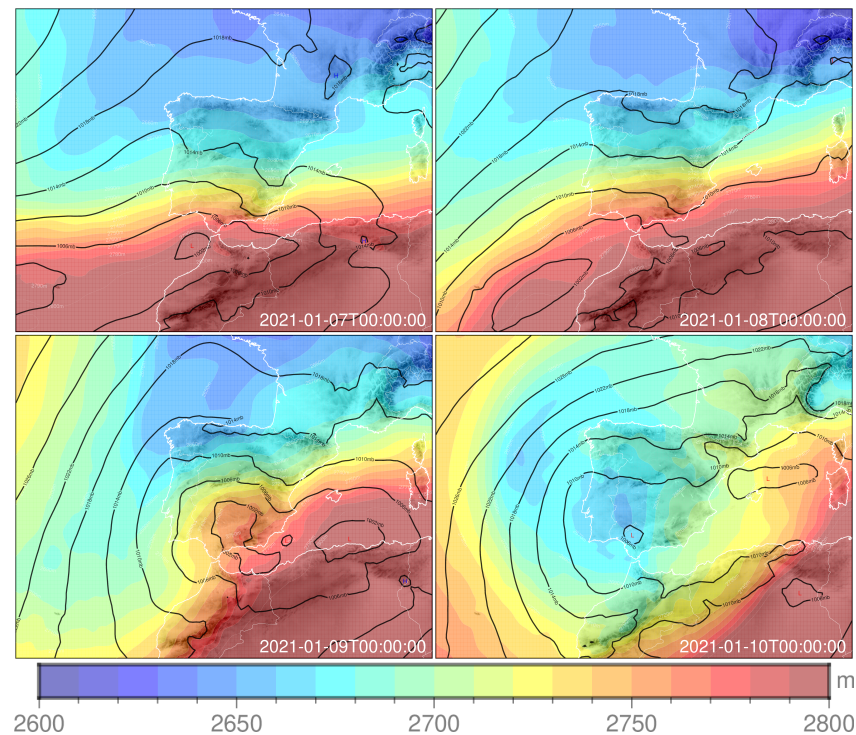


Figure 1. Maps of 600–850 hPa layer thickness (shaded) and sea level pressure (contours) associated with Storm Filomena on 7–10 January 2021 at 00:00 UTC.

2.2. Model Configuration

A set of simulations was performed with the WRF-Chem model (V3.9.1.1) [30,31]. The model setup was fixed for all experiments except for the microphysical configuration.

Regarding the general physical configuration, radiation was parameterized with the rapid radiative transfer model for global climate models (RRTMG) by Mlawer et al. [32], both for short- and long-wave radiation, updated every 30 min. The surface layer parameterization was solved with the Mesoscale Model MM5 scheme based on the similarity theory by Monin and Obukhov [33] and using the revised scheme of Jiménez et al. [34], while the *The unified NOAA LSM* option was used for the land surface calculation [35]. Four soil layers were considered in the land surface model, and the Yonsei University scheme was employed for the boundary layer [36], solved every time step ($bldt = 0$). Heat and moisture fluxes from the surface were activated ($isfflx = 1$), as well as the cloud effect to the optical depth in radiation ($icloud = 1$). Conversely, snow cover effects were deactivated ($ifsnw = 0$). Land-use and soil-category data came from WPS geogrid but with dominant categories recomputed ($surface_input_source = 1$). The urban canopy model was not considered ($sf_urban_physics = 0$), and the topographic surface wind correction from Jiménez and Dudhia [37] was turned on. Both feedback from the parameterized convection to the radiation schemes and SST update (every 6 h, coinciding with boundary conditions update) were also turned on. The simulations were run in two one-way nested domains, D01 and D02, having 9 and 3 km of horizontal grid resolution, respectively, and arranged as indicated in Figure 2. Regarding the cumulus physics, Grell 3D ensemble ($cu_physics = 5$; $cudt = 0$) was chosen to parameterize convection [38] in the coarse domain D01. For D02, no cumulus parameterization was used, considering its resolution to be within the convection-permitting zone. The output of the simulations for the coarser domain were used only to feed the finer simulations using a one-way nesting strategy. Data from an ERA-interim global atmospheric reanalysis was used to provide the simulations with the required initial and boundary conditions (every 6 h) [39].

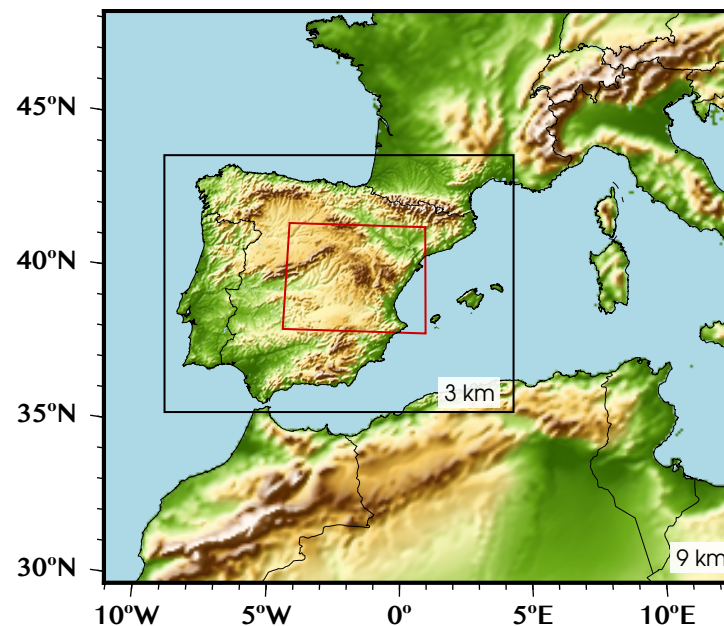


Figure 2. Overview of the parent domain D01 and the nested domain D02, employed in the simulations at 9 and 3 km of grid spacing, respectively. The red box shows the studied area, and the colors refer to terrain height.

2.3. Microphysics Setup

In the last two decades, double-moments microphysics approaches have been usually considered [40–42]. The increase in complexity accomplished when solving both the mixing ratio and the number concentration for the different hydrometeors leads to a more realistic treatment of the cloud droplets and ice crystals populations, which directly influence the cloud microphysics and, ultimately, the precipitation and radiative balance [43,44]. The Morrison et al. [45] microphysics scheme was chosen for the simulations in this work. It was implemented in the WRF model in such a way that it allowed a coupling with the chemistry module (WRF-Chem) [46,47], and was based on a double-moment approach for five types of hydrometeors (cloud droplets, cloud ice, rain, snow and hail/graupel), i.e., their mixing ratio and number concentration were validated. Hydrometeor size distributions were assumed to follow gamma functions; while Marshall–Palmer exponential functions ($\mu = 0$) were employed for the size distributions of precipitation species (rain, snow and graupel) and cloud ice. For cloud droplets, the shape parameter μ was a function of the predicted droplet number concentration [45].

For the purposes of this work, two different WRF-Chem configurations were considered. The first one is the prescribed aerosol configuration (PA from now on), and it is equivalent to using WRF alone. In this configuration, dry aerosols show a constant total concentration and are prescribed to follow a lognormal size distribution. In the same way as in the work of Morrison and Grabowski [48], a single mode is considered; the total number concentration of aerosols, N_t , is controlled by the *naer* parameter, which is adjustable in the WRF-Chem name list and defaults to 10^9 aerosols per kilogram of dry air. This parameter was modified in the interest of carrying out a sensitivity study in the way specified in Section 3.2. Ammonium sulfate was considered as the chemical species for the prescribed aerosols, and thus a fixed concentration of a given type of aerosol, with a hygroscopic growth factor of 0.5 [49], was prescribed every time and everywhere. Hence, the amount of aerosols that serve as potential CCN to form cloud droplets prior to their activation remains constant in the simulation [50]. In this prescribed case, the default parameterization of Abdul-Razzak and Ghan [51] calculates number, surface and mass fraction of activated aerosols by means of the maximum supersaturation and following the

Köhler theory. Given the CCN spectrum and the spectrum of updraft velocities, the droplet nucleation rate was calculated and the droplet number concentration predicted.

In the second approach (interactive aerosols, referred to as IAs), the dynamic core of WRF was coupled to a chemistry module [30]. The model simulates emission, transport, mixing, and chemical transformation of trace gases and aerosols simultaneously with the meteorology. The main advantage of employing WRF-chem with respect to using WRF alone is the possibility to perform an online calculation of the natural aerosol emission and transport. Specifically, the Goddard chemistry aerosol radiation and transport (GOCART) scheme [52] simulates major tropospheric aerosol components, including sulfate, dust, black carbon, organic carbon and sea salt aerosols, the latter being dominant in marine environments [53]. GOCART includes sea salt aerosol (SSA) emission as a function of the surface wind speed, initially introduced by Gong [54] and after modified to account for SST dependence and some other corrections [55]. For the emission, the dry size of the particles is considered but the scheme also includes their hygroscopic growth, dependent on relative humidity, according to the equilibrium parameterization by Gerber [56]. When using GOCART, the SSA are distributed in four different size bins with a mean radius of 0.3, 1.0, 3.2 and 7.5 μm , and [0.1, 0.5], [0.5, 1.5], [1.5, 5.0] and [5.0, 10.0] μm of upper and lower bin radii, respectively; the prescribed mode included in the Morrison microphysics parameterization, which was used in the PA simulations, is now replaced by the online calculated aerosol mass emission within each size bin. In addition, each chemical species is considered with its own hygroscopic parameter (see in Table 3 of Chin et al. [57] the hygroscopic growth factors at different RH as employed in GOCART), provided that the activation and hygroscopic growth are explicitly calculated, and the cloud droplet number concentration (CDNC) generated in the Abdul-Razzak and Ghan [51] approach is passed to the microphysics scheme [58]. Note that no anthropogenic emissions are taken into account.

In both cases, the ice nucleation is fixed as a function of temperature as described in Morrison and Gettelman [59] using the Cooper [60] formula. Hence, the aerosol number concentration does not influence the ice crystal number concentration in a direct manner, as it does with the cloud droplet number concentration, albeit it does influence the ice crystal concentration in an indirect way since the aerosol concentration regulates the cloud droplet concentration, which affects the microphysical processes in which ice crystals are involved, thus indirectly changing the ice crystal concentration. In the present version of the Morrison microphysics parameterization, ice multiplication by rime splintering is neglected [61].

All experiments ran from 3 January 2021 to 10 January 2021. Output was recorded every hour. No initial conditions for aerosol loading were used in the IA experiment. However, the almost five-day *spinup* period was enough to produce a reasonable aerosol load. No anthropogenic emissions were used. Therefore, only natural aerosols were taken into account.

3. Results

3.1. Effect of Interactive versus Prescribed Aerosols

First of all, the effect of interactive aerosols in the simulation of Storm Filomena was analyzed by direct comparison of interactive aerosols and the default prescribed aerosol simulations (PA1E9, hereunder PA throughout this subsection). Figure 3 shows the patterns of total precipitation (first row), rain (second row), snow (third row) and graupel (fourth row), accumulated during the study period (from 8 January 2021 07:00 UTC to 10 January 2021 07:00 UTC), for the IA (first column) and PA (second column) simulations, as well as their differences (third column).

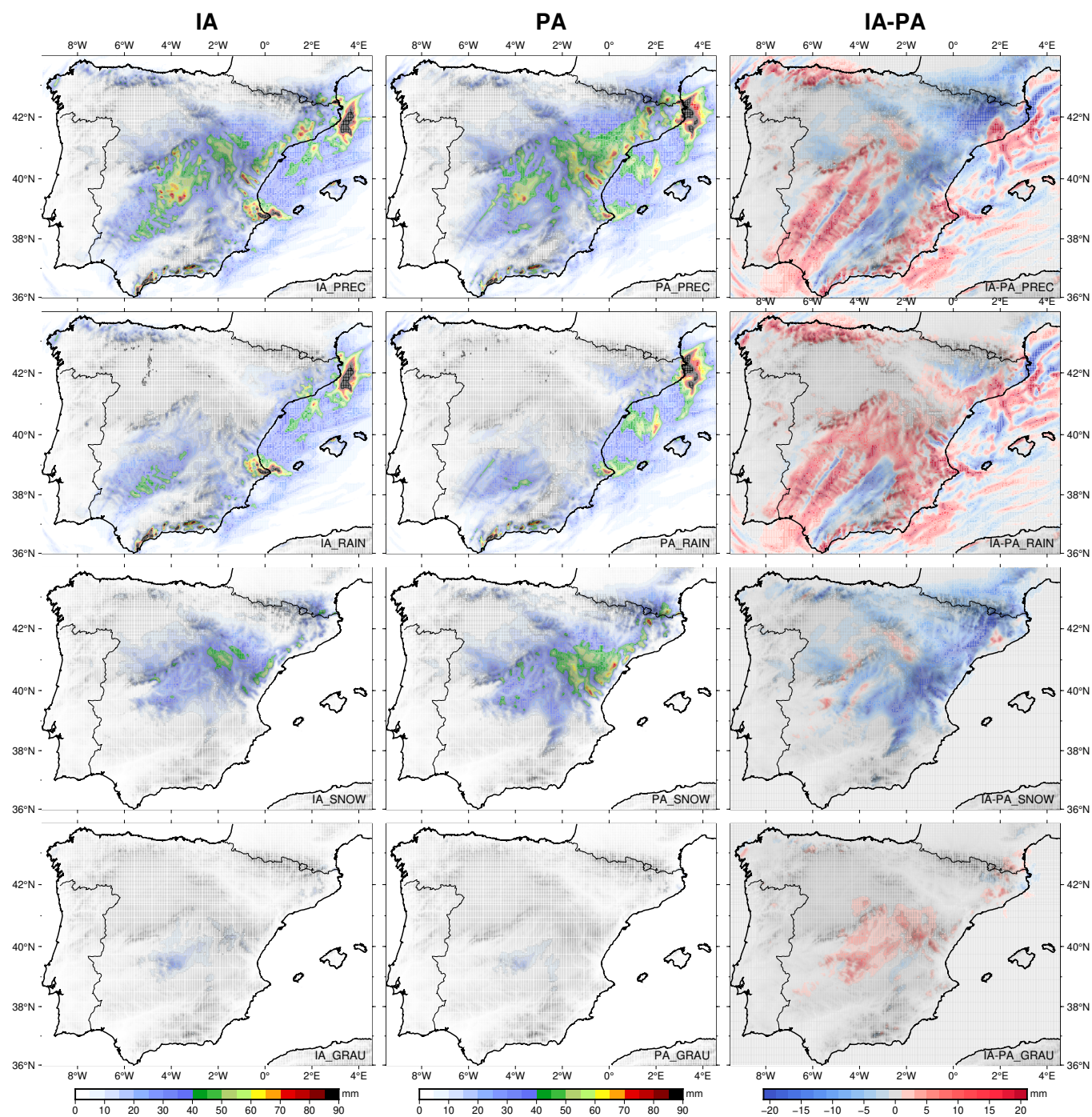


Figure 3. Maps of total precipitation (first row), rain (second row), snow (third row) and graupel (fourth row), for the IA (first column) and PA1E9 (default prescribed aerosols, second column) cases, as well as their differences (third column). The same color scales are employed for the first two columns—one per row—while a different scale is used for the differences.

Both simulations produced an intense precipitation event with amounts of total precipitation reaching 200 mm and snow accumulation larger than 90 mm. The precipitation to the south of the front was warm (rain), with snow to the north and in elevated areas to the south. Furthermore, due to the encounter with the cold air mass, two different sections of warm precipitation were formed: one of them brought warm moist air directly from southern locations where Storm Filomena was located. This released rain in the southern and mid latitudes of the IP. Moreover, a second branch of Filomena moved eastward and fed from the Mediterranean Sea moisture, causing intense precipitations in the eastern part of the IP. In fact, the most intense precipitation in the form of snow was due to the interaction of this moist air mass with the Iberian system mountains close to the East Coast. Graupel production formed near the frontal surface.

Regarding the differences between the IA and PA cases, while IA produces more rain both in western and eastern locations and little differences at the north of the front, the southern locations register less liquid precipitation in the IA case. Overall, 27.3% more rain was produced in the IA case. This was accompanied by an increase in the overall graupel production (74% more graupel in IA). However, this was largely compensated with the decrease in snow production. The snow in the IA case showed a 27% reduction. The total precipitation decreased 5% when interactive aerosols were introduced. Thus, in summary, introducing interactive aerosols leads to the production of less precipitation in the form of snow which, in this specific case of a winter storm, was the primary one; higher rain and graupel production was additionally observed. However, given that the total precipitation was not conserved, we can conclude that the differences shown are not the cause of a redistribution alone.

With the aim of diving into the causes of these differences, we first selected a spatial window to restrict the area under study: the area in which the snowfall was more intense (see red box in Figure 2). A land mask was also employed to remove sea grid cells. Then, the points were separated into bins according to their terrain height; 21 bins were created, containing points with heights from 0 to 2000 m above sea level (ASL) every 100 m. For each bin, the precipitation of the grid cells was averaged for each precipitation type. Figure 4 shows for each bin, the total precipitation split into rain, snow and graupel for both the IA (grey, black, blue and orange) and PA (red, white, yellow and green) simulations. The number of points within each bin is also depicted (salmon shading). Additionally, the percentage of each precipitation type is shown in the top bars.

From Figure 4 several insights can be drawn. First of all, we observe that for the bins in which the major part of the points are classified, the total precipitation is slightly higher in the PA case than in the IA case, a result in line with that of Figure 3. In the same direction, rain and graupel production keeps being higher in the IA simulation. For the extreme heights (0 to 100 m and above 1700 m or so), too few points are collected within a bin to draw any conclusion. Regarding the bars showing the percentage of the total precipitation that is produced in each form (rain, snow or graupel), the IA simulation consistently predicts less snow. Although it is partially compensated by a higher production of graupel, the freezing precipitation is lower in the IA case for every height bin. This last fact shows that the signal is independent of the height, which seems to indicate that its origin lies in microphysical causes rather than in thermodynamical ones because the effect of an increase in the snow level due to a thermodynamical effect would be imperceptible once the snow level was reached in both simulations.

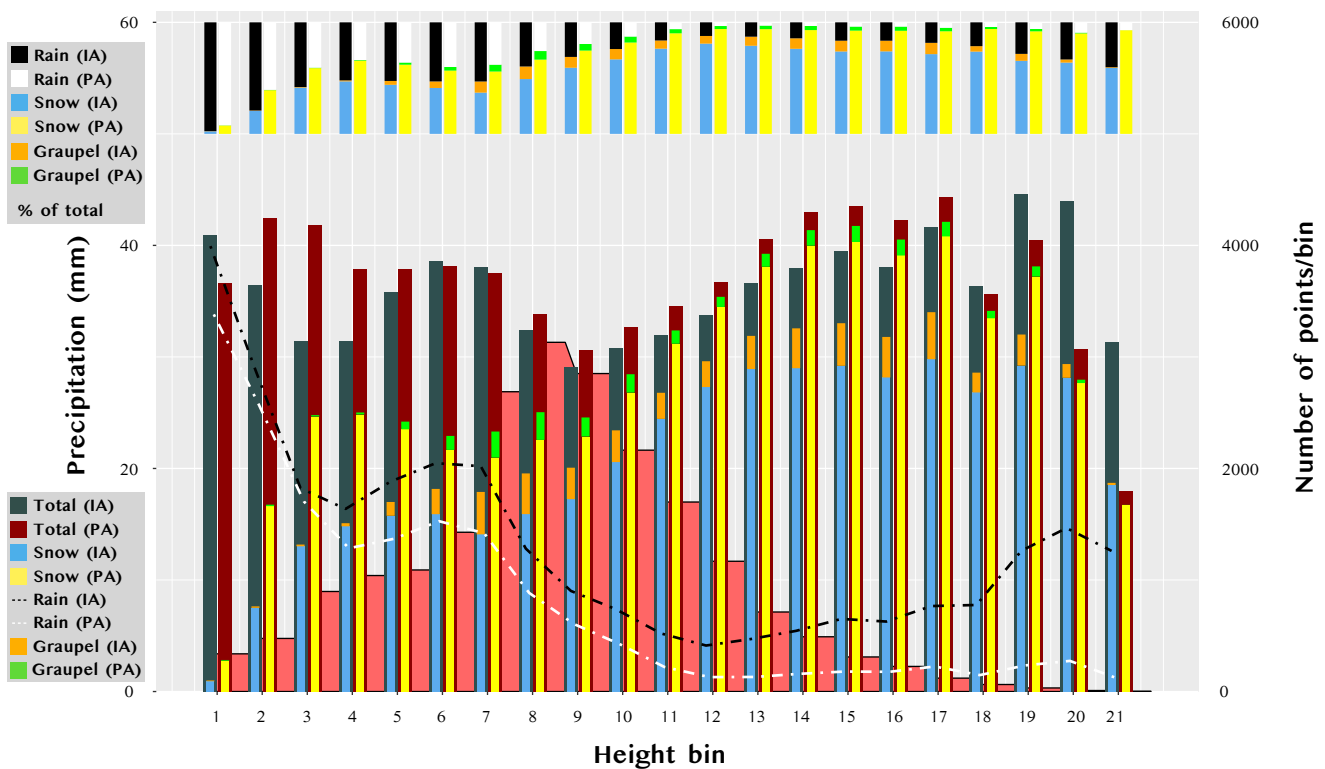


Figure 4. Plot with total precipitation, rain, snow and graupel quantities, accumulated in the study period, averaged to the points within each terrain height bin for IAs (**left**) and PAs (**right**), organized into bars with ascending heights. Dark grey and dark red colors are used for the bars that mark the total precipitation of the IA and PA cases, respectively. The blue (yellow) bars refer to the accumulated snow for the IA (PA) case, whereas the black (white) line refers to the accumulated rain for the IA (PA) case, and the orange (green) bars show the accumulated graupel for the IA (PA) case. The bars above separate the percentage of the total precipitation in each precipitable form (IA: rain in black, snow in blue and graupel in orange; PA: rain in white, snow in yellow and graupel in green).

In order to complete the analysis of the differences introduced by the use of interactive aerosols in the simulation of Storm Filomena, the vertical distribution of the different hydrometeors is showcased in Figure 5. A temporal average of each hydrometeor is performed for the time steps of the study period in which the total precipitation is above 0.5 mm, and again, they are grouped into height bins. The vertical distribution of the water vapor mixing ratio, temperature, cloud water mixing ratio, ice water mixing ratio, cloud droplet number concentration and ice crystal number concentration for the IA (first column) and PA1E9 (second column) cases, as well as their differences (third column), are shown. These plots are complemented with the ones in Figure 6, showing rain, snow and graupel mixing ratios with the same disposition as the hydrometeors of Figure 5. When showing air temperature, the freezing level (blue line) is shown along with the zone of maximum efficiency of the WBF process (delimited with two red lines), i.e., the zone limited by the temperatures for which the difference between equilibrium vapor pressure curves of ice and liquid water drops to 90% of its maximum ($-18.5^{\circ}\text{C} < T < -7.6^{\circ}\text{C}$).

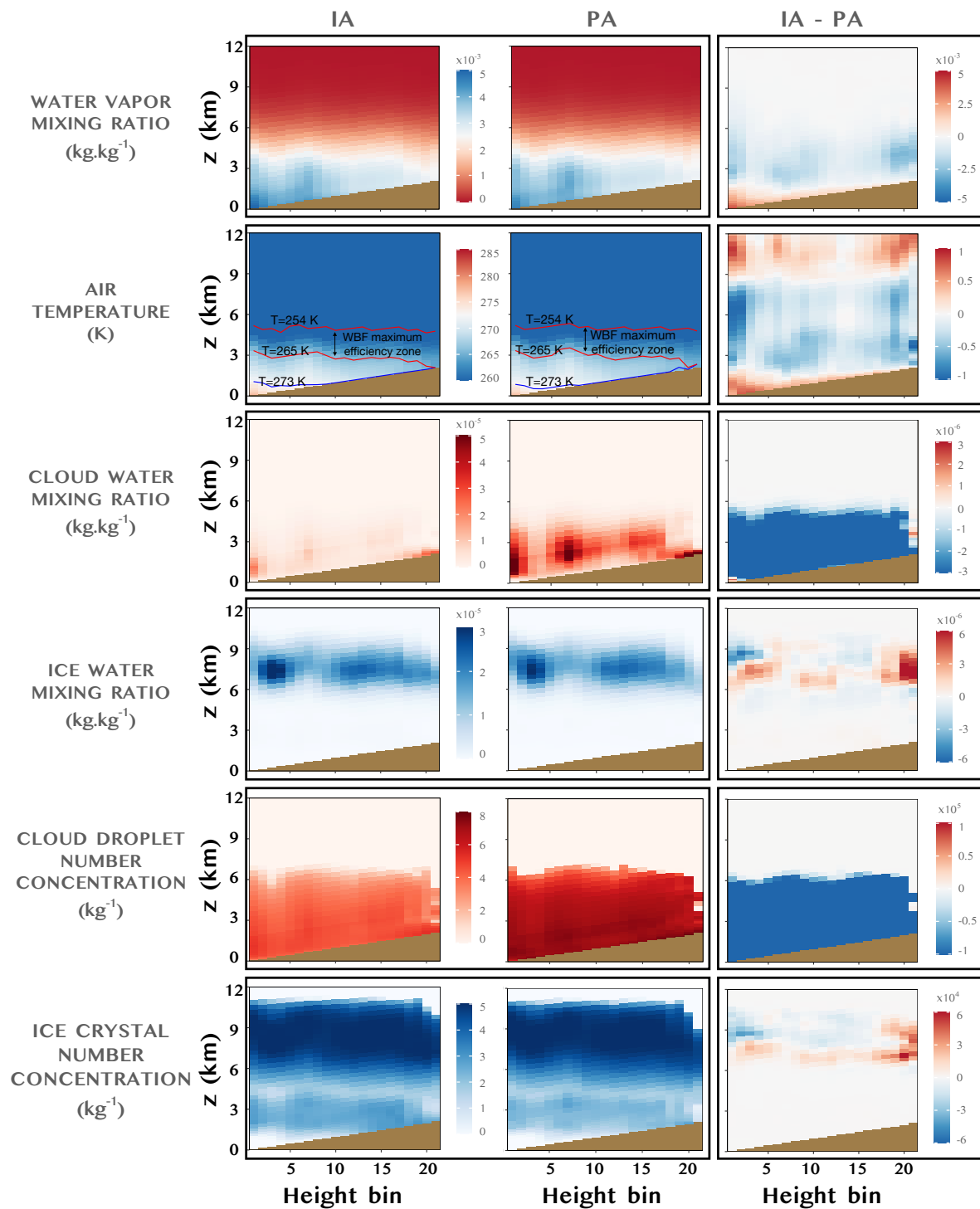


Figure 5. Vertical distribution of water vapor mixing ratio (WVMR, in kg/kg), temperature (T , in K), cloud water mixing ratio (CWMR, in kg/kg), ice water mixing ratio (IWMR, in kg/kg), cloud droplet number concentration (CDNC, in kg^{-1}) and ice crystal number concentration (ICNC, in kg^{-1}) for the IA (left column) and PA (center column) cases, as well as their differences (right column), grouped by terrain height bins. Hydrometeor fields are temporally averaged to those times in which the total precipitation is above 0.5 mm.

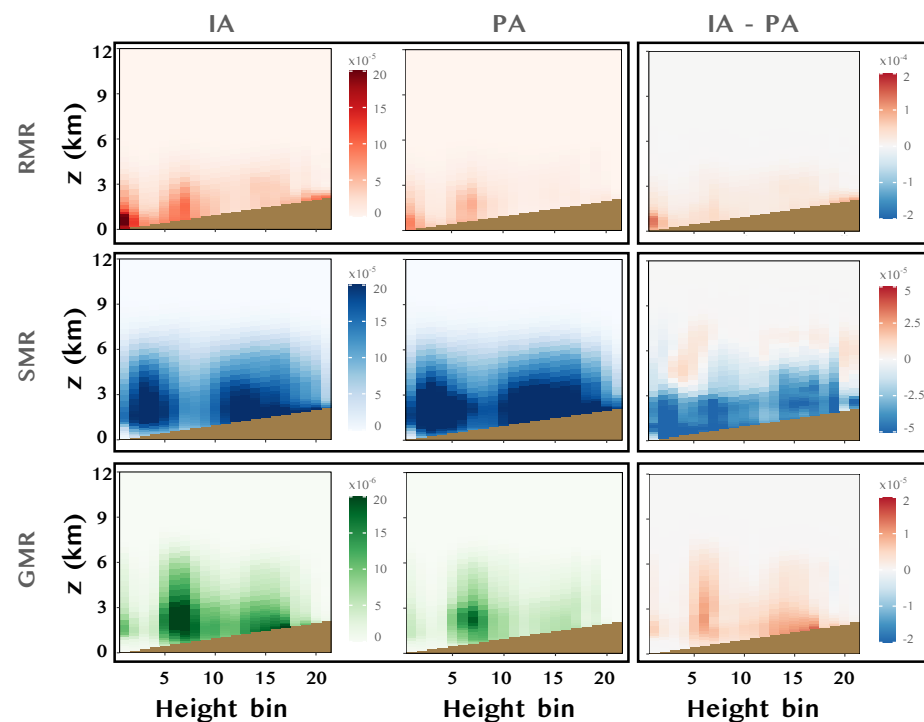


Figure 6. The same as in Figure 5, but for rain (RMR), snow (SMR) and graupel (GMR) mixing ratios, all in kg/kg.

From the first two columns of Figures 5 and 6, we see that rain mainly falls in the height bins of 0 to 100 m ASL, which correspond to the coastal points to the east of the IP, where the moist air mass coming from the Mediterranean region encounters land. There is also rainfall in higher locations corresponding to continental points of lower latitudes, where the snow level is still high. When moving inward, precipitation is released as snow. A part of the precipitation is formed as graupel close to the warm front (not shown), a zone of higher updraft, which is in line with the theory of Braham [2]. The most intense graupel production appears on points with terrain height around the snow level, provided that these points induce orographically induced convection with strong updrafts that favour the formation of graupel. In this case, there exists a depletion of ice crystals due to their rapid conversion into graupel when the freezing contact of supercooled water-cloud droplets with them takes place. According to Figure 5, the depletion of ice crystals is also strong in the zone of maximum WBF efficiency, where a horizontal band of lesser concentration of ice crystals may be clearly seen. Regarding the differences between IAs and PAs, IAs lead to a lower production of snow, compensated—only partially, as demonstrated later—with an increase of rainfall and graupel formation. Graupel is formed in zones of increased LWC, a result in line with the theory of graupel formation introduced by Matsuo et al. [20], analyzed in more detail in Section 3.2. For heights well above the freezing level, snow is the principal precipitating hydrometeor, which is more abundant in the PAs than in the IA simulation. Concerning the temperature distribution, a difference of approximately 1 degree is reached below the freezing level. There, the IA simulation produces a higher temperature, which is probably related to the increased aerosols dry radius and hygroscopicity, producing a more rapid hygroscopic growth and the release of latent heat. In the PA, this hygroscopic growth is expected to be slower and less effective provided that a lower hygroscopic growth factor and smaller aerosols are considered. This air temperature difference also implies a difference in the water vapor mixing ratio as extracted from the Clausius–Clapeyron equation. For heights above the freezing level, and specially in the zone of maximum WBF efficiency, the latent heat of freezing and deposition comes into play, leading to higher temperatures in the PA case, in which these processes are more effective than in the IA case: in PAs we observe a higher cloud water mixing ratio—i.e., of supercooled water. As these

are smaller and more numerous cloud droplets than those of the IA case, their evaporation is more prone, thus enhancing the WBF process, and their availability for ice riming growth in mid tropospheric levels is also higher. Thus, in the PA case, the increased supercooled liquid water content produces the mentioned increase in the efficiency of snow production, and conversely reduces the rain and graupel production rates. The 5% decrease in total precipitation observed in Figure 3 for the IA simulation may be caused by the decreased efficiency of the WBF process. The riming efficiency, in case of increasing with decreased aerosols, is too weak to balance the decrease in WBF efficiency. The reduction in snow production in the IA case is partially compensated by an increase in the liquid precipitation in the easternmost locations of the IP. In the rest of the domain, temperatures are too low for the warm processes to compensate the defect of snow production.

On the basis of this analysis, it may be concluded that, aside from a decrease in the total precipitation, a much more intense redistribution exists from snow into rain and graupel when interactive aerosols are introduced. Further, we have showcased the fact that this redistribution, far from having its origin in spatial or dynamical causes, is due to the increased efficiency of rain and graupel formation along with the decreased efficiency in snow formation, which seem to be directly related to the supercooled liquid water content, materialized in the cloud droplet number concentration and mean cloud droplet size. Furthermore, it has been concluded that the temperature and water vapor content differences are, rather than causes, consequences of the different efficiencies of these microphysical processes, without prejudice to the possibility of existing positive feedbacks that may further increase these efficiency differences. To complete the discussion, one further step is taken concerning the number of aerosols prescribed in the PA simulation. In line with what was mentioned above, the droplet number is much higher in the PA case and seems to be related with the number of aerosols. Provided that the number of activated aerosols depends directly on the number concentration of dry aerosols, the role of the prescribed aerosol concentration has to be analyzed.

3.2. Sensitivity of Snow Formation Efficiency to the Number Concentration of Aerosols

The prescribed aerosol (PA) concentration in the experiment showed before is 10^9 aerosol per kilogram of dry air that is approximately $N_t \rho_d$ of 1225 aerosol per cm^3 . A quick calculation on AI experiments to transform the aerosol loading, expressed in mass terms, into number of aerosols, yields a value in the range of 1 to 10 aerosols per cm^3 of dry air. Therefore, the IA concentration is a thousand times lower than the PA experiment.

Aside from other factors, such as the different hygroscopic growth factors considered in the two cases or the different aerosols size distribution directly related to their activation as CCN, the total number of aerosols is, according to the literature, the most determinant factor in the efficiency of precipitation formation. The typical aerosol number concentrations for continental regions are in the range of 10^2 to 10^4 cm^{-3} , while for marine regions, the concentrations are generally lower, ranging from 10 to 10^3 cm^{-3} . However, these concentrations can vary depending on several factors, such as location, time of year, and meteorological conditions. However, as visited in the introduction, uncertainty still exists about the key factors regulating precipitation in mixed-phase clouds. Among them, the number of cloud droplets and the availability of supercooled water are usually considered to be the most important factors regulating the precipitation initiation in mixed-phase clouds, thus the sensitivity study carried out in this section. With this aim, six additional prescribed (fixed) aerosol simulations were carried out, in which the total aerosol concentration was varied, ranging $N_t \rho_d$ from 1.225 cm^{-3} (PA1E6) to 1225 cm^{-3} (PA, the default one already analyzed, from now on is referred to as PA1E9), having the intermediate ones 6.125 cm^{-3} (PA5E6), 12.25 cm^{-3} (PA1E7), 61.25 cm^{-3} (PA5E7), 122.5 cm^{-3} (PA1E8) and 612.5 cm^{-3} (PA5E8).

The results of this sensitivity study are summarized in Table 1, which shows the spatially—both vertically and horizontally—and temporally averaged values of air temperature (T), water vapor mixing ratio (WVMR), cloud water mixing ratio (CWMR), liquid

water content (LWC), ice water mixing ratio (IWMR), cloud droplet number concentration (CDNC), cloud droplet radius (CDR), ice crystal number concentration (ICNC), rain mixing ratio (RMR), snow mixing ratio (SMR) and graupel mixing ratio (GMR) for each simulation.

Table 1. Summary of the spatial—horizontal and vertical below 9 km—and temporal average values of the mixing ratio of different hydrometeors: temperature (T, in K), water vapor mixing ratio (WVM, in $\text{kg}\cdot\text{kg}^{-1} \times 10^6$), cloud water mixing ratio (CWM, in $\text{kg}\cdot\text{kg}^{-1} \times 10^6$), liquid water content (LWC, in $\text{g}\cdot\text{m}^{-3}$), ice water mixing ratio (IWM, in $\text{kg}\cdot\text{kg}^{-1} \times 10^6$), cloud droplet number concentration (CDNC, in $\text{kg}^{-1} \times 10^{-6}$), cloud droplet radius (CD, in μm), ice crystal number concentration (ICNC, in $\text{kg}^{-1} \times 10^{-6}$), rain mixing ratio (RM, in $\text{kg}\cdot\text{kg}^{-1} \times 10^6$), snow mixing ratio (SM, in $\text{kg}\cdot\text{kg}^{-1} \times 10^6$) and graupel mixing ratio (GM, in $\text{kg}\cdot\text{kg}^{-1} \times 10^6$). The N_t column refers to the total aerosol number concentration (in $\text{kg}^{-1} \times 10^{-6}$), which is variable in the IA simulation.

Sim	N_t	T	WVM	CWM	LWC	IWM	CDNC	CDR	ICNC	RM	SM	GM
IA	[0–5]	255.7	2154.6	2.4 (2)	0.002 (9)	4.7 (1)	0.01 (7)	32.0	0.02 (25)	28.3	85.7	6.1
PA1E6	1	255.8	2169.6	2.4 (6)	0.003 (0)	4.6 (9)	0.02 (4)	29.0	0.02 (25)	26.5	91.0	5.3
PA5E6	5	255.8	2174.0	3.3	0.004 (0)	4.7 (2)	0.07 (6)	21.7	0.02 (27)	25.2	93.5	5.3
PA1E7	10	255.8	2172.4	4.0	0.004 (8)	4.7 (1)	0.14 (7)	18.6	0.02 (25)	24.2	94.6	5.1
PA5E7	50	255.8	2170.8	6.4	0.007 (8)	4.7 (3)	0.70 (3)	13.0	0.02 (29)	20.8	98.4 (8)	4.9
PA1E8	100	255.8	2171.1	7.6	0.009 (3)	4.6 (8)	1.31 (1)	11.1	0.02 (26)	18.7	98.5 (5)	4.5
PA5E8	500	255.8	2175.4	10.6	0.013 (0)	4.7 (5)	4.85 (2)	8.1	0.02 (32)	15.4	105.1	3.9
PA1E9	1000	255.8	2169.7	11.6	0.014 (2)	4.6 (9)	7.75 (5)	7.1	0.02 (30)	14.0	105.6	3.7

Table 1 and Figure 7 show the total accumulated precipitation, rain, graupel and snow across the domain during the study period versus the number of aerosols in every experiment. Total precipitation remains almost constant for all experiments, just a small increase. However, there appears to be a clear redistribution from snow into rain and graupel. This is in agreement with what was found when introducing interactive aerosols with respect to the PA1E9 case. Simulations reducing the prescribed aerosol concentration, from the default $N_{i\rho_d} = 1225 \text{ cm}^{-3}$ to the $N_{i\rho_d} = 1.225 \text{ cm}^{-3}$ employed in the PA1E6 simulation, give more graupel and less rain. The snow production rates are thus drastically inhibited with decreasing prescribed background aerosols, and the rain and graupel production are largely amplified. The total precipitation achieved in the PA1E6 case is now very close to that produced in the IA case (a 0.8% increase). Moreover, we appreciate that the gradual increase in the aerosol concentration progressively reduces the differences with the PA1E9 case. Provided that the ice water mixing ratio and ice crystal number concentration are left practically unaltered when aerosol concentration is modified, we need to focus on the supercooled water content, both its mixing ratio and the size and number concentration of its associated hydrometeor: cloud droplets. With increased aerosols, the water vapor and ice water mixing ratios are nearly conserved except for random variations with no pattern; the same applies to the number concentration of ice nuclei. The conservation of the former indicates that the same amount of water vapor is converted into hydrometeors for all simulations, whether it is condensed into cloud droplets or deposited into ice crystals. As expected due to the dependence of the Cooper formula on the temperature alone, the ice content suffers small variations from one simulation to another, mainly related to the temperature differences and to the changes in the efficiency of the microphysical processes. Furthermore, increased aerosols augment the cloud water mixing ratio, as expected according to the Albrecht lifetime effect, and hence the liquid water content is also increased. In the same direction but with stronger magnitude, is the increase of the cloud droplet number concentration when the aerosol concentration is raised, which causes a reduction in the cloud droplet mean radius for larger aerosol concentrations. As expected, the rain mixing ratio is decreased according to the increased droplet number concentration and increased mean droplet radius, and conversely, the snow mixing ratio is increased for the

reason explained above: more numerous and smaller cloud droplets provide the supply for a more efficient WBF process, as discussed in the introduction. With respect to the graupel, the LWC is high enough to favour its formation in all the simulations, as discussed below, and hence the decrease in the cloud droplet mean radius with increasing aerosols dominates the effect, making the formation of graupel less efficient.

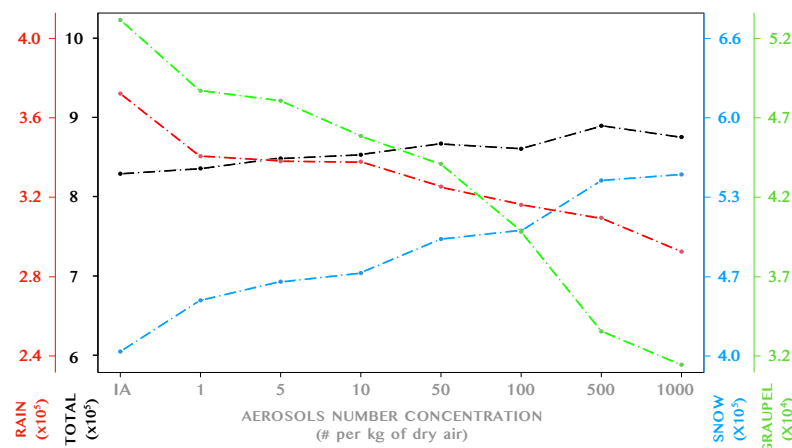


Figure 7. Total precipitation (black), rain (red), snow (blue) and graupel (green) summed across the red window shown in Figure 2 and accumulated to the study period for all the experiments as a function of aerosol number concentration (x-axis). IA in the x-axis represents the results for the IA experiment.

According to the values presented in Table 1, as well as to the progressive reduction in the IA and PA differences in precipitation observed in Figure 7 when the aerosol number concentration is decreased from the default PA (PA1E9) case to the one closest to IAs (PA1E6), the simulations show that the supercooled water governs the microphysical processes that induce the observed differences, both through its content (liquid water content) and physical manifestation (size and number concentration of cloud droplets). Specifically, and as discussed in the introduction, the formation of snow is enhanced when high amounts of liquid water are found, being especially true when it is distributed in a high number of cloud droplets, thus showing a small mean droplet radius. On the one hand, the WBF process is more effective in the case of more and smaller droplets due to the increased evaporation of cloud droplets. Recall that the evaporation rate is inversely proportional to the droplet radius because of the increased surface tension in plane surfaces. On the other hand, although the ice riming process should be less effective provided smaller supercooled droplets are formed, the fact that more supercooled water is available in the form of droplets that rime in the surface of ice crystals compensates for it. According to the literature, further investigation into this topic is required.

On another note, when aerosol concentration is decreased, rain production is more effective, provided that the mean droplet size is higher and precipitable sizes more easily reached by C–C processes. In addition, graupel production is more effective due to the increased droplet size, as shown in the CDR column of Table 1. In fact, according to the numbers provided in Matsuo et al. [20], the droplet sizes are above the threshold of effective graupel production (10 μm) in all the simulations with aerosol concentrations below $N_t\rho_d = 122.5$ aerosols per cubic centimeter of dry air. The LWC threshold, around $0.4 \text{ g}\cdot\text{m}^{-3}$, is exceeded in all simulations, thus being the mean droplet size that is the most determinant factor in the production of graupel. Therefore, the lower the aerosol concentration is, the larger the droplet size and the more effective the graupel formation process.

Furthermore, in light of the vertical distributions presented in Figure 5, rain production seems to be limited to the heights below the freezing level and above the freezing level but out of the zone of highest efficiency of WBF, where temperatures are high enough to maintain rainfall production due to the effect of C–C processes, and ice crystal presence is

low enough to present low probabilities of heterogeneous nucleation. However, the most intense differences between the IA and PA1E9 rain production rates are precisely below the freezing level, where the IA case shows increased rainfall production efficiencies due to the increased droplet mean radius and the subsequent high efficiency of the C–C processes. In the PA1E9 case, these processes are highly inefficient due to the high amount of cloud droplets with small sizes, which enhance the presence of supercooled liquid water droplets at higher levels by the effect of convective lifting. This enhanced presence of small supercooled droplets in higher levels is precisely what increases the WBF process efficiency. When aerosols are progressively decreased, the mean droplet radius is gradually increased, the C–C processes efficiency—and hence the rain production—raised, the supercooled water availability at high levels—and thus the snow production efficiency—diminished and the graupel production boosted. This also explains the differences in the temperature vertical distributions observed in Figure 5: at heights below the freezing level, the IA simulation releases the latent heat of condensation more locally because of the increased efficiency in the hygroscopic growth, an effect that is not achieved in any prescribed aerosol simulation (see temperature column of Table 2). In the PA1E9 simulation, the cloud droplets absorb water vapor in a more steady and slower rate and more easily reach higher levels with temperatures below freezing, where they stop growing and start evaporating according to the WBF theory. It is precisely at these heights that the WBF shows its highest efficiency where PA1E9 releases more latent heat—provided that the absolute value of the latent heat of deposition is higher than that of the latent heat of evaporation—with respect to IA due to the increased efficiency of the WBF process when compared to that of the IA case, which translates into the increased temperature shown in the PA1E9 simulation for levels above the snow level.

Table 2. The same as in Table 1, but for the maximum values.

Sim	N_t	T	WVM	CWM	LWC	IWM	CDNC	CDR	ICNC	RM	SM	GM
IA	[0–5]	285.6	9171.6	563.8	0.6 (9)	180.2	3.8 (7)	32.6	0.7 (12)	3524.1	2676.9	3024.1
PA1E6	1	285.2	8855.2	573.1	0.7 (0)	164.1	3.9 (4)	32.6	0.7 (05)	2919.4	2789.9	2366.0
PA5E6	5	285.2	8902.1	633.5	0.7 (7)	160.8	5.0	31.2	0.7 (00)	2582.2	3631.5	2156.0
PA1E7	10	285.2	8878.1	754.5	0.9 (2)	167.2	10.0	26.2	0.7 (12)	2867.8	2890.8	1969.6
PA5E7	50	285.5	8965.0	911.6	1.1 (2)	162.7	49.9	16.3	0.7 (06)	2201.5	3558.2	2549.4
PA1E8	100	285.5	8959.1	925.0	1.1 (3)	167.3	99.6	13.1	0.7 (01)	2159.2	3294.0	2186.0
PA5E8	500	285.9	9160.6	1163.5	1.4 (3)	178.7	498.4	8.2	0.7 (06)	1986.8	3440.6	2454.6
PA1E9	1000	285.5	8873.7	1321.8	1.6 (2)	163.2	993.5	6.8	0.7 (09)	2179.9	3320.4	2076.9

We concluded earlier that the increase in the ice crystal growth efficiency for higher aerosol concentrations leads to enhanced snowfall, which is counterbalanced with the rainfall and graupel production increase, although just partially. This provoked an increase in the total precipitation for higher aerosol concentrations. Provided that the water vapor mixing ratio is practically conserved for all simulations, we conclude that the increase in the mean droplet size, which causes a decrease in the snow formation efficiency, does not increase the rain and graupel forming efficiencies in the same proportion. Thus, an excess of supercooled water should exist with decreased aerosols, especially in mid and high levels, due to this lower efficiency of precipitation production, probably covered by the larger defect of cloud water precisely due to this increase in the mean droplet size. Moreover, the change in precipitation between the PA1E6 and the IA simulations is higher than expected according to the differences in cloud droplet number concentration and mixing ratio that they show. With a view to inquiry into this fact, we analyze both the spatial correlation of the accumulated snow patterns in the different simulations, as well as their the mean of their differences. The results of this analysis are shown in Figure 8, in which

the correlation (upper diagonal) and mean bias (lower diagonal) are presented for every pair of simulations.

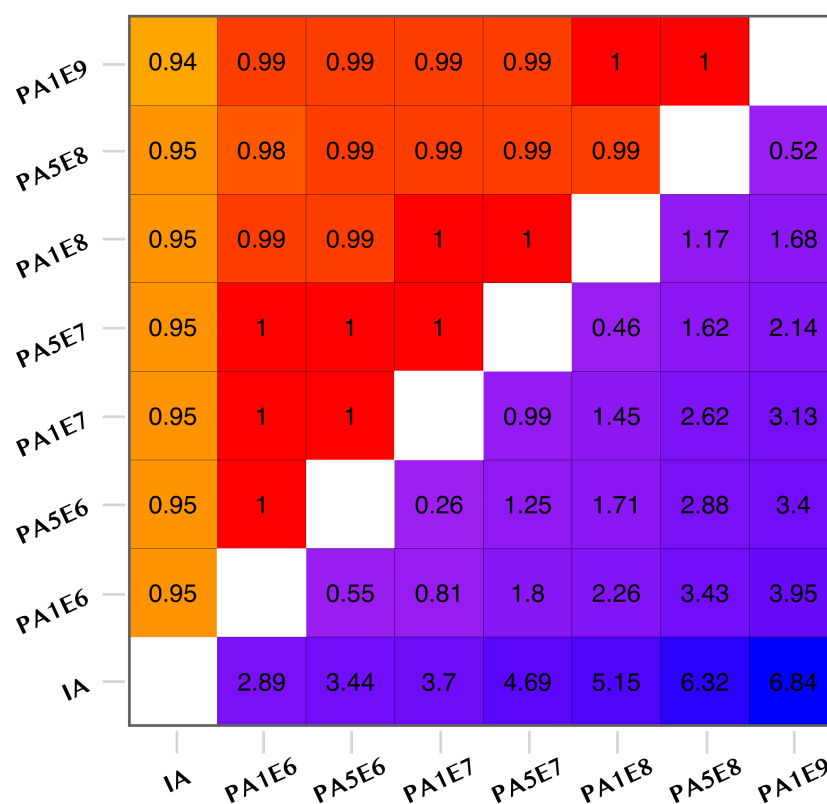


Figure 8. Correlations (upper diagonal) and mean differences (lower diagonal) between the accumulated snow fields of the different simulations.

Figure 8 reveals that increasing the prescribed aerosols produces an increase in the mean bias, i.e., enhances the snowfall overall. The correlations are nearly the same for all prescribed aerosol simulations. Therefore, increasing aerosols leave the snow pattern mostly unaltered but increases the snow precipitation. Conversely, the introduction of interactive aerosols induces the appearance of a different snow pattern that is not reproduced even when prescribed aerosols are reduced to the same order of magnitude of that reached in the interactive aerosol simulation. Therefore, this confirms that the spatial and temporal variation of the aerosol field introduces significant differences in spatial distribution of the snowfall and that using the prescribed aerosols always produces a similar pattern, with the aerosol concentration regulating the magnitude of the snowfall.

3.3. Evaluation of Simulations

The previous sections analyzed the differences in precipitation production when interactive aerosols approach and several fixed aerosol concentrations are employed. In this section, we analyze the ability of the various configurations of the model to reproduce the observations. Calculating the aerosol concentration from the meteorological fields when compared to prescribing a constant concentration of them in space and time stands as a more physically consistent approach and a step towards a better reproduction of the microphysics processes in the model. However, it could be the case that, due to the high number of parameterizations that the models include, the reproduction of a particular event was not better with the introduction of interactive aerosols. We used a database with the precipitation registered during the study period at different meteorological stations. These data, obtained from AEMET (*Agencia Estatal de Meteorología* of Spain), contain daily accumulated precipitation at the locations shown in Figure 9.

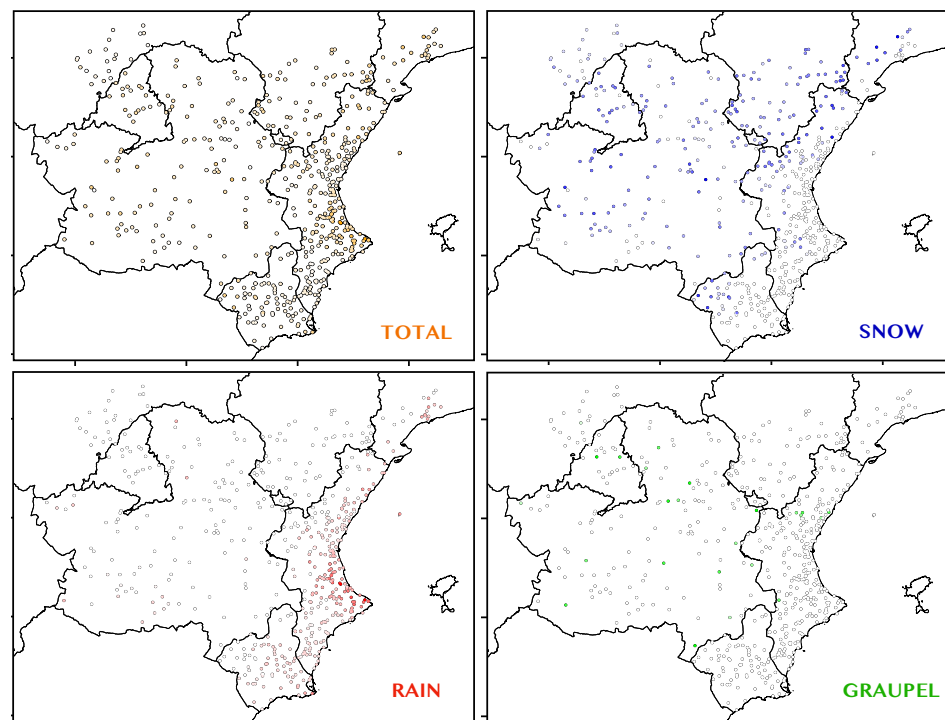


Figure 9. Locations of the stations in the data set employed for the validation of simulations. Colors indicate precipitation registered at each station during the study period, scaled to the maximum of each precipitation type (**top left**: total precipitation, **top right**: snow, **bottom left**: rain and **bottom right**: graupel). Data obtained under direct request to AEMET.

Provided that the graupel field seems spatially inconsistent with uneven values in close locations, probably due to the lack of real graupel observations, we will exclude this type of precipitation from the individual validation although it is accounted in the total precipitation. For the fields of total precipitation, rain and snow accumulated in the study period, both the RMSE (root mean square error) and the spatial correlation against the observations data set are presented in Table 3. For each station included in the data set, the model grid point that is closest to its location is selected for the validation.

Table 3. For each simulation, RMSE (RM), spatial correlation (CR) and mean bias (BS) of total precipitation (TPCP), rain and snow fields with respect to the observations data set are shown.

Sim	PTCP RM	RAIN RM	SNOW RM	TPCP CR	RAIN CR	SNOW CR	TPCP BS	RAIN BS	SNOW BS
IA	17.99	17.81	15.29	0.64	0.78	0.66	5.01	9.26	−4.70
PA1E6	16.11	15.34	15.07	0.67	0.79	0.66	4.03	6.42	−2.82
PA5E6	16.31	15.25	15.24	0.66	0.79	0.66	4.60	6.41	−2.21
PA1E7	16.45	15.33	15.28	0.65	0.78	0.66	4.69	6.43	−2.08
PA5E7	16.39	14.72	15.32	0.65	0.79	0.66	4.67	5.75	−1.33
PA1E8	16.59	14.49	15.39	0.63	0.79	0.66	4.32	5.02	−0.80
PA5E8	17.13	14.25	15.75	0.61	0.78	0.67	5.08	4.37	0.90
PA1E9	16.70	13.74	15.51	0.61	0.79	0.68	4.27	3.42	1.08

For the total precipitation, no significant differences seem to exist between simulations to conclude which one performs better with respect to the observations. Whereas lower RMSE is reproduced with decreasing prescribed aerosols, a steep increase in this statistic is introduced when interactive aerosols come into play with respect to the PA1E6 simulation. This is complemented by the fact that a higher spatial correlation is accomplished

with decreasing aerosol concentration; again, there exists a decrease in the correlation when going from PA1E6 to IA. At the individual level, both rain and snow show higher RMSE when interactive aerosols are used. For rain, the RMSE increases with decreasing aerosols, especially for the IA case. Conversely, for snow, RMSE decreases when increasing aerosols although in a non significant level. Correlation is almost constant for both rain and snow with varying aerosol concentrations. According to the bias, the interactive aerosols approach leads to an overestimation of rain along with an underestimation of snow. Thus, from these results, we could conclude that using prescribed aerosols with a low concentration (PA1E6) is the best choice when addressing the simulation of Storm Filomena.

As a last step, we employ the square cell methodology introduced in Pravia-Sarabia et al. [62] to prevent the influence of a double penalty effect. A square cell of 3×3 grid points is selected, and the best modelled value within the square cell around the grid point corresponding to the location of the station is taken for each gauge included in the validation data set to validate against the precipitation registered at the station. This validation procedure is designed to account for the fact that extreme precipitation, such as that induced by Filomena, is difficult to reproduce due to the high influence of local orographic factors; in addition, especially in high resolution simulations, the reproduction of precipitation peaks in grid cells close to but not coincident with the station location is considered as successful. The results of this validation approach are shown in Table 4.

Table 4. The same as in Table 3 but with the square cell method to select the grid point around the station location in which the model value is closest to the observation.

Sim	TPCP RM	RAIN RM	SNOW RM	TPCP CR	RAIN CR	SNOW CR	TPCP BS	RAIN BS	SNOW BS
IA	11.16	12.13	13.09	0.83	0.88	0.77	2.51	5.86	−3.97
PA1E6	10.02	10.68	12.53	0.86	0.89	0.78	2.01	4.07	−2.64
PA5E6	10.43	10.74	12.58	0.85	0.89	0.77	2.54	4.11	−2.14
PA1E7	10.43	10.62	12.51	0.85	0.89	0.77	2.61	4.10	−2.02
PA5E7	11.23	10.67	12.40	0.82	0.89	0.78	2.70	3.61	−1.42
PA1E8	11.70	10.46	12.28	0.80	0.89	0.78	2.62	3.12	−0.99
PA5E8	12.53	10.37	12.35	0.77	0.89	0.79	3.14	2.67	0.26
PA1E9	12.32	10.12	12.17	0.77	0.89	0.79	2.55	1.97	0.49

With the square cell method, the validation results are slightly different: the RMSE of total precipitation is diminished if aerosol concentration is decreased, although for IA it is moderately higher than for PA1E6, PA5E6 and PA1E7. However, rain and snow root mean square errors are both increased. With regard to the correlation, it is increased for decreased aerosols for the total precipitation field, but the correlation of the individual components, rain and snow, is maintained with varying aerosols. These results show that as long as we allow for a displacement in the reproduction of the precipitation value at the station with the square cell validation approach, the total precipitation field is better simulated with interactive aerosols than with the default prescribed aerosols—lower RMSE and higher spatial correlation of the total precipitation. However, we appreciate a worsening in the reproduction of the individual components in the IA case. Definitely, the best results according to the validation with observations are achieved with the prescribed aerosols simulation PA1E6—prescribed aerosols with low concentration—which minimizes the RMSE and maximizes the correlation. This can be attributable to a higher spatial variability of precipitation in the IA experiment.

At this point, it should be noted that the collection of meteorological data in this type of situation is not optimal, especially in areas where the weather stations are not prepared for this extreme cold situation. This is why the quality of the data may be compromised. However, the large amount of data (meteorological stations) used can

minimize this problem. Nevertheless, it is important to know that although it seems that there are simulations that can better explain the observed field, the differences in skill scores are very small. This, together with other aspects already noted, such as the uncertainty of the model associated to physical parameterizations, dynamics, boundary meteorological conditions, as well as the uncertainty in the observational database itself, do not allow us to distinguish that one simulation (or aerosol configuration) is differentially better than the others.

4. Conclusions

This work analyzed through numerical simulations the role of aerosols in the formation of different types of precipitation during the Filomena storm, one of the extreme snow events in the Iberian Peninsula in recent years. The simulations were carried out by means of the WRF-Chem model using two-moment microphysics. The experiments consisted of a set of simulations where the prescribed aerosols (PAs) varied over a wide range of concentrations and an experiment using interactive aerosol simulation (IA).

The introduction of interactive aerosols produced a 5% decrease in total precipitation with respect to the simulation with default prescribed aerosols ($N_t\rho_d = 1225 \text{ cm}^{-3}$). The difference decreased to 0.8% when the prescribed concentration became smaller and smaller ($N_t\rho_d = 1.225 \text{ cm}^{-3}$). All the PA simulations presented a very similar precipitation pattern, varying only in intensity. However, the IA simulation presented a more differentiated pattern.

The main change observed was the redistribution of the total precipitation in the different meteors. As aerosol concentration increased, the amount of snowfall rose considerably at the expense of reduced graupel and rainfall. Changes in simulations with prescribed aerosols in snow can be greater than 25%, with the IA simulation producing the least amount of snow. The loss of graupel production in the most extreme case can reach values of around 75%, while in rainfall it reaches 28%. Considering that the aerosol concentration in IA varies from 1 to 5 cm^{-3} , it can be assured that the aerosol concentration is fundamental to simulate the partitioning of meteor formation.

The relationship between snow production and aerosol concentration has its origin in the efficiency of the WBF process. Having a higher aerosol concentration leads to a higher CCN formation and therefore a higher number of droplets. This fact leads to a smaller droplet radius which decreases the efficiency in the production of raindrops (inhibited C-C processes) and graupel. Therefore, a larger amount of supercooled water is available which enhances the WBF process. Ice riming efficiency is either not affected by changes in aerosol concentrations or not enough affected to counteract the increased WBF efficiency. Under low concentrations of large supercooled droplets (IA), ice riming is the predominant mechanism, which also gives rise to graupel embryos. Note that although rain efficiency is increased with IA, total precipitation is decreased given that temperatures were low in the main part of the studied territory and therefore snow was the leading meteor.

Although meteorological records in this type of situation may pose various uncertainties (freezing devices, non-optimal measuring devices, etc.), a comparison of modeled and observational data was performed. The total precipitation field was better reproduced with interactive aerosols than with the default prescribed aerosols; however, we saw a worsening in the reproduction of the individual components, specifically rain and snow, in the IA case. Lowering the prescribed aerosols from PA1E9 to PA1E6 yielded the best results when compared to observations, both in RMSE and correlation.

According to biases (see Tables 3 and 4) and the fact that while default PA simulations overestimate snow in continental locations (see Appendix A), the IA simulation underestimates it and overestimates rain type precipitation in near-maritime locations. Aerosol concentration could probably be underestimated in some areas. This fact can be attributable to a defect in the GOCART scheme use in this work or the exclusion of other aerosols such as anthropogenic ones.

In summary, a correct estimation of aerosols can be of vital importance when estimating the spatial distribution of precipitation as well as its partitioning into the different hydrometeors. Improved aerosol–atmosphere interactive systems should lead to better predictions with respect to using prescribed aerosol concentrations. This may be of vital importance, especially in a simulation of extreme events in mixed systems. It should be added that this improved simulation of aerosol concentration may not only be important for precipitation-related processes (microphysics) but also for the direct and semi-direct effects that aerosols have on radiation.

However, it is important to know that there are many factors that can contribute to minor shifts in the performance that will then affect aerosol cloud interaction processes, such as ambient environmental conditions, the simple representation of aerosols (GOCART), the incomplete treatment of ACI processes in mixed-phase cloud systems or secondary ice production. In addition, the introduction of natural aerosols alone could be a deficient approach for an event with these characteristics; the zone of influence of Storm Filomena reached continental locations where anthropogenic may have some impact. This was not included in this study because the GOCART anthropogenic emissions of black carbon and organic carbon are taken from a global data set with 1° horizontal resolution from more than twenty years ago [63]. Therefore, an improvement in the representation of these aerosol sources should lead to a better estimation of the aerosols population as well as the use of more sophisticated natural aerosol production and transport models. Moreover, in this study, aerosols are considered as a whole, even in the IA case, where the different aerosol types can be analyzed separately. Provided the different ice nucleating ability and freezing critical temperatures of different chemical species [64], a sensitivity study isolating each species could shed some light on the particular contribution of each one. For this case study, sea salt aerosols should have exerted the greatest influence over precipitation formation in coastal locations of the IP, while organic and black carbon arising from anthropogenic activity may have been important in the snowfall over the continental territory by action of Storm Filomena.

Author Contributions: E.P.-S. carried out the WRF simulations and performed the calculations of this paper; E.P.-S., J.P.M. and A.H.-M. contributed to the design of the simulations, and both A.H.-M. and J.P.M. helped E.P.-S. with their analysis; E.P.-S., A.H.-M., J.P.M., J.J.G.-N. and P.J.-G. provided substantial expertise on the topic that contributed to an insightful understanding of the underlying physical processes; E.P.-S. wrote the paper, and all authors contributed to reviewing the text. All authors have read and agreed to the published version of the manuscript.

Funding: This study was supported by the Spanish Ministry of the Economy and Competitiveness/*Agencia Estatal de Investigación* and the European Regional Development Fund (ERDF/FEDER) through projects ACEX-CGL2017-87921-R and ECCE/PID2020-115693RB-I00. AHM thanks his predoctoral contract FPU18/00824 to the *Ministerio de Ciencia, Innovación y Universidades* of Spain.

Data Availability Statement: The simulations included and analyzed herein have been performed with WRF-Chem model (V3.9.1.1). The source code for this model can be downloaded from the WRF Users Page https://www2.mmm.ucar.edu/wrf/users/download/get_source.html (accessed on 12 November 2020). The data object of this work contains different simulations and exceeds the size available in the online repositories. Please note that the simulations raw output files are available upon request to the authors.

Acknowledgments: The authors would like to thank Juan Andrés García Valero and the Spanish *Agencia Estatal de Meteorología* for providing the data used for the validation of the simulations. Authors are also thankful to the WRF-Chem development community.

Conflicts of Interest: The authors declare no conflict of interest.

Abbreviations

The following abbreviations are used in this manuscript:

PA	Prescribed Aerosols
IA	Interactive Aerosols
CCN	Cloud Condensation Nuclei
LWC	Liquid Water Content
WBF	Wegener-Bergeron-Findeisen
WRF	Weather Research Forecast Model

Appendix A

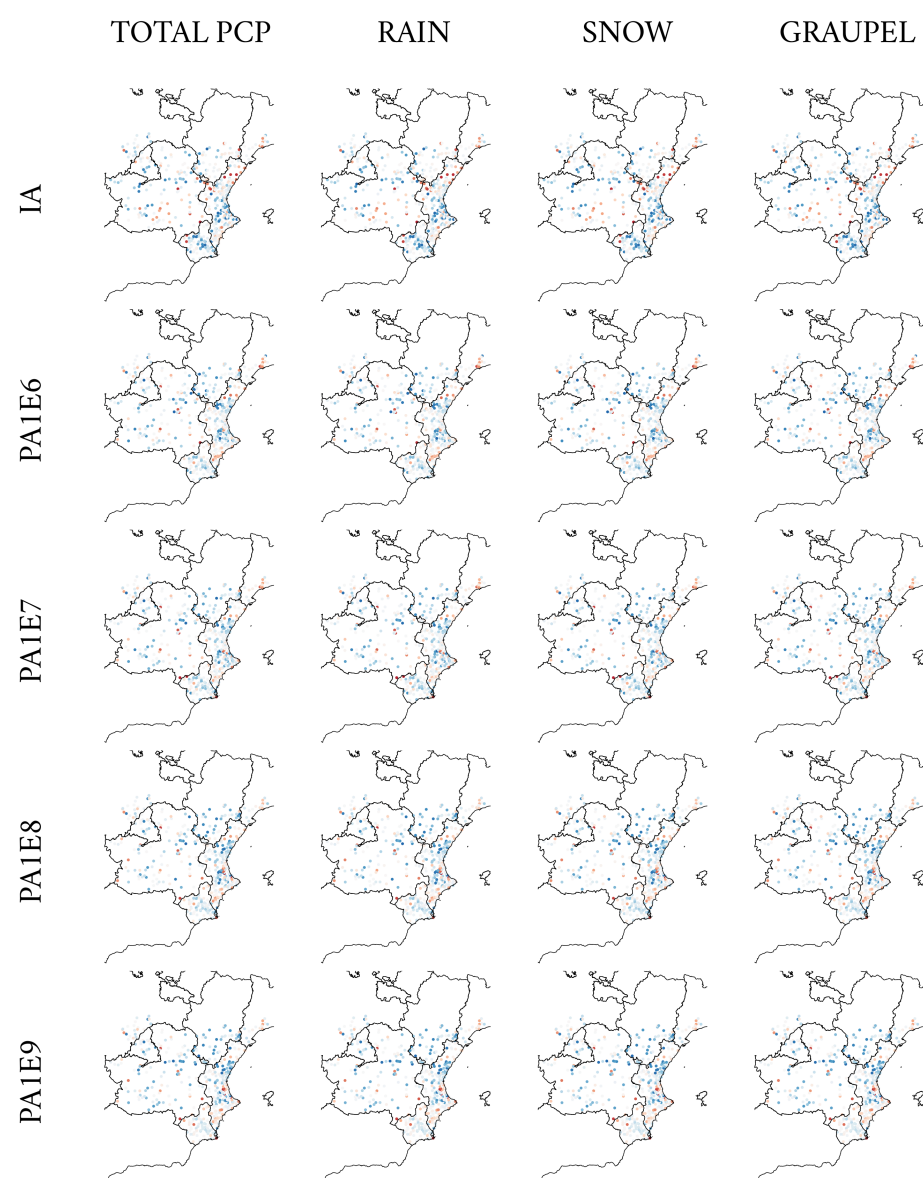


Figure A1. Biases from validation with stations, calculated as the model-reproduced values (using the square cell methodology with 3×3 points of square cell size) minus the observed values of precipitation. Blue (red) colors indicate overestimation (underestimation) of the observations by the model, i.e., higher (lower) modeled values than the observed ones.

References

1. Korolev, A.; McFarquhar, G.; Field, P.R.; Franklin, C.; Lawson, P.; Wang, Z.; Williams, E.; Abel, S.J.; Axisa, D.; Borrmann, S.; et al. Mixed-Phase Clouds: Progress and Challenges. *Meteorol. Monogr.* **2017**, *58*, 5.1–5.50. [\[CrossRef\]](#)
2. Braham, R.R. Meteorological bases for precipitation development. *Bull. Am. Meteorol. Soc.* **1968**, *49*, 343–353. [\[CrossRef\]](#)
3. Beard, K.V.; Ochs, H.T., III. Warm-rain initiation: An overview of microphysical mechanisms. *J. Appl. Meteorol. Climatol.* **1993**, *32*, 608–625. [\[CrossRef\]](#)
4. Wegener, A. *Thermodynamik der Atmosphäre*; JA Barth: Leipzig, Germany, 1911.
5. Bergeron, T. On the physics of clouds and precipitation. In Proceedings of the 5th Assembly UGGI, Lisbon, Portugal, 1935; pp. 156–180.
6. Findeisen, W. Kolloid-meteorologische Vorgänge bei Neiderschlags-bildung. *Meteor. Z.* **1938**, *55*, 121–133.
7. Twomey, S.; Squires, P. The influence of cloud nucleus population on the microstructure and stability of convective clouds. *Tellus* **1959**, *11*, 408–411. [\[CrossRef\]](#)
8. Albrecht, B.A. Aerosols, Cloud Microphysics, and Fractional Cloudiness. *Science* **1989**, *245*, 1227–1230. [\[CrossRef\]](#)
9. Bigg, E. The formation of atmospheric ice crystals by the freezing of droplets. *Q. J. R. Meteorol. Soc.* **1953**, *79*, 510–519. [\[CrossRef\]](#)
10. Kanji, Z.A.; Ladino, L.A.; Wex, H.; Boose, Y.; Burkert-Kohn, M.; Cziczo, D.J.; Krämer, M. Overview of ice nucleating particles. *Meteorol. Monogr.* **2017**, *58*, 1.1–1.33. [\[CrossRef\]](#)
11. Morrison, H.; van Lier-Walqui, M.; Fridlind, A.M.; Grabowski, W.W.; Harrington, J.Y.; Hoose, C.; Korolev, A.; Kumjian, M.R.; Milbrandt, J.A.; Pawlowska, H.; et al. Confronting the challenge of modeling cloud and precipitation microphysics. *J. Adv. Model. Earth Syst.* **2020**, *12*, e2019MS001689. [\[CrossRef\]](#)
12. Reisin, T.; Levin, Z.; Tzivion, S. Rain production in convective clouds as simulated in an axisymmetric model with detailed microphysics. Part II: Effects of varying drops and ice initiation. *J. Atmos. Sci.* **1996**, *53*, 1815–1837. [\[CrossRef\]](#)
13. Fan, J.; Leung, L.R.; Rosenfeld, D.; DeMott, P.J. Effects of cloud condensation nuclei and ice nucleating particles on precipitation processes and supercooled liquid in mixed-phase orographic clouds. *Atmos. Chem. Phys.* **2017**, *17*, 1017–1035. [\[CrossRef\]](#)
14. Muhlbauer, A.; Hashino, T.; Xue, L.; Teller, A.; Lohmann, U.; Rasmussen, R.M.; Geresdi, I.; Pan, Z. Intercomparison of aerosol-cloud-precipitation interactions in stratiform orographic mixed-phase clouds. *Atmos. Chem. Phys.* **2010**, *10*, 8173–8196. [\[CrossRef\]](#)
15. Borys, R.D.; Lowenthal, D.H.; Cohn, S.A.; Brown, W.O. Mountaintop and radar measurements of anthropogenic aerosol effects on snow growth and snowfall rate. *Geophys. Res. Lett.* **2003**, *30*, GL016855. [\[CrossRef\]](#)
16. Xiao, H.; Yin, Y.; Chen, Q.; Zhao, P. Impact of aerosol and freezing level on orographic clouds: A sensitivity study. *Atmos. Res.* **2016**, *176–177*, 19–28. [\[CrossRef\]](#)
17. Hallett, J.; Mossop, S. Production of secondary ice particles during the riming process. *Nature* **1974**, *249*, 26–28. [\[CrossRef\]](#)
18. Reinking, R.F. Formation of graupel. *J. Appl. Meteorol.* **1975**, *14*, 745–754. [\[CrossRef\]](#)
19. Scott, B.C.; Hobbs, P.V. A theoretical study of the evolution of mixed-phase cumulus clouds. *J. Atmos. Sci.* **1977**, *34*, 812–826. [\[CrossRef\]](#)
20. Matsuo, T.; Mizuno, H.; Masataka, M.; Yoshinori, Y. Requisites of graupel formation in snow clouds over the sea of Japan. *Atmos. Res.* **1994**, *32*, 55–74. [\[CrossRef\]](#)
21. Kumjian, M.R.; Ganson, S.M.; Ryzhkov, A.V. Freezing of raindrops in deep convective updrafts: A microphysical and polarimetric model. *J. Atmos. Sci.* **2012**, *69*, 3471–3490. [\[CrossRef\]](#)
22. Sun, J.; Shi, Z.; Chai, J.; Xu, G.; Niu, B. Effects of mixed phase microphysical process on precipitation in a simulated convective cloud. *Atmosphere* **2016**, *7*, 97. [\[CrossRef\]](#)
23. Thériault, J.M.; Stewart, R. On the effects of vertical air velocity on winter precipitation types. *Nat. Hazards Earth Syst. Sci.* **2007**, *7*, 231–242. [\[CrossRef\]](#)
24. Ramelli, F.; Henneberger, J.; David, R.O.; Bühl, J.; Radenz, M.; Seifert, P.; Wieder, J.; Lauber, A.; Pasquier, J.T.; Engelmann, R.; et al. Microphysical investigation of the seeder and feeder region of an Alpine mixed-phase cloud. *Atmos. Chem. Phys.* **2021**, *21*, 6681–6706. [\[CrossRef\]](#)
25. Khain, A. Notes on state-of-the-art investigations of aerosol effects on precipitation: A critical review. *Environ. Res. Lett.* **2009**, *4*, 015004. [\[CrossRef\]](#)
26. Letcher, T.; Cotton, W.R. The effect of pollution aerosol on wintertime orographic precipitation in the Colorado Rockies using a simplified emissions scheme to predict CCN concentrations. *J. Appl. Meteorol. Climatol.* **2014**, *53*, 859–872. [\[CrossRef\]](#)
27. Saleeby, S.M.; Cotton, W.R.; Lowenthal, D.; Messina, J. Aerosol impacts on the microphysical growth processes of orographic snowfall. *J. Appl. Meteorol. Climatol.* **2013**, *52*, 834–852. [\[CrossRef\]](#)
28. Ilotoviz, E.; Khain, A.P.; Benmoshe, N.; Phillips, V.T.; Ryzhkov, A.V. Effect of aerosols on freezing drops, hail, and precipitation in a midlatitude storm. *J. Atmos. Sci.* **2016**, *73*, 109–144. [\[CrossRef\]](#)
29. Agencia Estatal de Meteorología. Informe Sobre el Episodio Meteorológico de Fuertes Nevadas y Precipitaciones Ocasionadas por Borrasca Filomena y Posterior Ola de Frío. 2021. Available online: http://www.aemet.es/documentos/es/conocermas/recursos_en_linea/publicaciones_y_estudios/estudios/Informe_episodio_filomena.pdf (accessed on 11 November 2012).
30. Grell, G.A.; Peckham, S.E.; Schmitz, R.; McKeen, S.A.; Frost, G.; Skamarock, W.C.; Eder, B. Fully coupled “online” chemistry within the WRF model. *Atmos. Environ.* **2005**, *39*, 6957–6975. [\[CrossRef\]](#)

31. Skamarock, W.; Klemp, J.; Dudhia, J.; Gill, D.; Barker, D.; Wang, W.; Powers, J. *A Description of the Advanced Research WRF Version 3*; NCAR: Boulder, CO, USA, 2008; Volume 27, pp. 3–27.
32. Mlawer, E.J.; Taubman, S.J.; Brown, P.D.; Iacono, M.J.; Clough, S.A. Radiative transfer for inhomogeneous atmospheres: RRTM, a validated correlated-k model for the longwave. *J. Geophys. Res. Atmos.* **1997**, *102*, 16663–16682. [[CrossRef](#)]
33. Monin, A.S.; Obukhov, A.M. Basic laws of turbulent mixing in the surface layer of the atmosphere. *Contrib. Geophys. Inst. Acad. Sci. USSR* **1954**, *151*, e187.
34. Jiménez, P.A.; Dudhia, J.; González-Rouco, J.F.; Navarro, J.; Montávez, J.P.; García-Bustamante, E. A Revised Scheme for the WRF Surface Layer Formulation. *Mon. Weather Rev.* **2012**, *140*, 898–918. [[CrossRef](#)]
35. Mitchell, K. The Community Noah Land-Surface Model (LSM). User's Guide. Recover. Volume 7. 2005. Available online: http://www.emc.ncep.noaa.gov/mmb/gcp/ldas/noahlsn/ver_2 (accessed on 20 July 2022).
36. Hong, S.Y.; Noh, Y.; Dudhia, J. A new vertical diffusion package with an explicit treatment of entrainment processes. *Mon. Weather Rev.* **2006**, *134*, 2318–2341. [[CrossRef](#)]
37. Jiménez, P.A.; Dudhia, J. Improving the representation of resolved and unresolved topographic effects on surface wind in the WRF model. *J. Appl. Meteorol. Climatol.* **2012**, *51*, 300–316. [[CrossRef](#)]
38. Grell, G.A.; Dévényi, D. A generalized approach to parameterizing convection combining ensemble and data assimilation techniques. *Geophys. Res. Lett.* **2002**, *29*, 38–1. [[CrossRef](#)]
39. Berrisford, P.; Dee, D.; Poli, P.; Brugge, R.; Fielding, M.; Fuentes, M.; Kållberg, P.; Kobayashi, S.; Uppala, S.; Simmons, A. *The ERA-Interim Archive Version 2.0*; ECMWF: Reading, UK, 2011; p. 23.
40. Morrison, H.; Curry, J.; Khvorostyanov, V. A new double-moment microphysics parameterization for application in cloud and climate models. Part I: Description. *J. Atmos. Sci.* **2005**, *62*, 1665–1677. [[CrossRef](#)]
41. Lim, K.S.S.; Hong, S.Y. Development of an effective double-moment cloud microphysics scheme with prognostic cloud condensation nuclei (CCN) for weather and climate models. *Mon. Weather Rev.* **2010**, *138*, 1587–1612. [[CrossRef](#)]
42. Grabowski, W.W.; Morrison, H. Untangling microphysical impacts on deep convection applying a novel modeling methodology. Part II: Double-moment microphysics. *J. Atmos. Sci.* **2016**, *73*, 3749–3770. [[CrossRef](#)]
43. Grabowski, W.W. Indirect impact of atmospheric aerosols in idealized simulations of convective–radiative quasi equilibrium. *J. Clim.* **2006**, *19*, 4664–4682. [[CrossRef](#)]
44. Gettelman, A.; Morrison, H.; Santos, S.; Bogenschutz, P.; Caldwell, P. Advanced two-moment bulk microphysics for global models. Part II: Global model solutions and aerosol–cloud interactions. *J. Clim.* **2015**, *28*, 1288–1307. [[CrossRef](#)]
45. Morrison, H.; Thompson, G.; Tatarskii, V. Impact of cloud microphysics on the development of trailing stratiform precipitation in a simulated squall line: Comparison of one-and two-moment schemes. *Mon. Weather Rev.* **2009**, *137*, 991–1007. [[CrossRef](#)]
46. Chapman, E.G.; Gustafson, W.I., Jr.; Easter, R.C.; Barnard, J.C.; Ghan, S.J.; Pekour, M.S.; Fast, J.D. Coupling aerosol-cloud-radiative processes in the WRF-Chem model: Investigating the radiative impact of elevated point sources. *Atmos. Chem. Phys.* **2009**, *9*, 945–964. [[CrossRef](#)]
47. Gustafson, W.I., Jr.; Chapman, E.G.; Ghan, S.J.; Easter, R.C.; Fast, J.D. Impact on modeled cloud characteristics due to simplified treatment of uniform cloud condensation nuclei during NEAQS 2004. *Geophys. Res. Lett.* **2007**, *34*, GL030021.
48. Morrison, H.; Grabowski, W.W. Comparison of Bulk and Bin Warm-Rain Microphysics Models Using a Kinematic Framework. *J. Atmos. Sci.* **2007**, *64*, 2839–2861. [[CrossRef](#)]
49. Petters, M.D.; Kreidenweis, S.M. A single parameter representation of hygroscopic growth and cloud condensation nucleus activity. *Atmos. Chem. Phys.* **2007**, *7*, 1961–1971. [[CrossRef](#)]
50. Wang, Y.; Fan, J.; Zhang, R.; Leung, L.R.; Franklin, C. Improving bulk microphysics parameterizations in simulations of aerosol effects. *J. Geophys. Res. Atmos.* **2013**, *118*, 5361–5379.
51. Abdul-Razzak, H.; Ghan, S.J. A parameterization of aerosol activation: 2. Multiple aerosol types. *J. Geophys. Res. Atmos.* **2000**, *105*, 6837–6844.
52. Chin, M.; Rood, R.B.; Lin, S.J.; Müller, J.F.; Thompson, A.M. Atmospheric sulfur cycle simulated in the global model GOCART: Model description and global properties. *J. Geophys. Res. Atmos.* **2000**, *105*, 24671–24687. [[CrossRef](#)]
53. Hoarau, T.; Barthe, C.; Tulet, P.; Claeys, M.; Pinty, J.P.; Bousquet, O.; Delanoë, J.; Vié, B. Impact of the generation and activation of sea salt aerosols on the evolution of Tropical Cyclone Dumile. *J. Geophys. Res. Atmos.* **2018**, *123*, 8813–8831. [[CrossRef](#)]
54. Gong, S.L. A parameterization of sea-salt aerosol source function for sub- and super-micron particles. *Glob. Biogeochem. Cycles* **2003**, *17*, 2079.
55. Bian, H.; Froyd, K.; Murphy, D.M.; Dibb, J.; Darmenov, A.; Chin, M.; Colarco, P.R.; da Silva, A.; Kucsera, T.L.; Schill, G.; et al. Observationally constrained analysis of sea salt aerosol in the marine atmosphere. *Atmos. Chem. Phys.* **2019**, *19*, 10773–10785. [[CrossRef](#)]
56. Gerber, H.E. *Relative-Humidity Parameterization of the Navy Aerosol Model (NAM)*; Technical Report; Naval Research Lab: Washington, DC, USA, 1985.
57. Chin, M.; Ginoux, P.; Kinne, S.; Torres, O.; Holben, B.N.; Duncan, B.N.; Martin, R.V.; Logan, J.A.; Higurashi, A.; Nakajima, T. Tropospheric aerosol optical thickness from the GOCART model and comparisons with satellite and Sun photometer measurements. *J. Atmos. Sci.* **2002**, *59*, 461–483. [[CrossRef](#)]
58. Yahya, K.; Glotfelty, T.; Wang, K.; Zhang, Y.; Nenes, A. Modeling regional air quality and climate: Improving organic aerosol and aerosol activation processes in WRF/Chem version 3.7.1. *Geosci. Model Dev.* **2017**, *10*, 2333–2363. [[CrossRef](#)]

59. Morrison, H.; Gettelman, A. A New Two-Moment Bulk Stratiform Cloud Microphysics Scheme in the Community Atmosphere Model, Version 3 (CAM3). Part I: Description and Numerical Tests. *J. Clim.* **2008**, *21*, 3642–3659. . 2008JCLI2105.1. [[CrossRef](#)]
60. Cooper, W.A., Ice Initiation in Natural Clouds. In *Precipitation Enhancement—A Scientific Challenge*; American Meteorological Society: Boston, MA, USA, 1986; pp. 29–32. [[CrossRef](#)]
61. Morrison, H.; Milbrandt, J.A. Parameterization of Cloud Microphysics Based on the Prediction of Bulk Ice Particle Properties. Part I: Scheme Description and Idealized Tests. *J. Atmos. Sci.* **2015**, *72*, 287–311. [[CrossRef](#)]
62. Pravia-Sarabia, E.; Halifa-Marín, A.; Gómez-Navarro, J.J.; Palacios-Peña, L.; Jiménez-Guerrero, P.; Montávez, J.P. On the role of aerosols in the production of orographically-induced extreme rainfall in near-maritime environments. *Atmos. Res.* **2022**, *268*, 106001. [[CrossRef](#)]
63. Cooke, W.; Liousse, C.; Cachier, H.; Feichter, J. Construction of a $1^\circ \times 1^\circ$ fossil fuel emission data set for carbonaceous aerosol and implementation and radiative impact in the ECHAM4 model. *J. Geophys. Res. Atmos.* **1999**, *104*, 22137–22162. [[CrossRef](#)]
64. Murray, B.; O'sullivan, D.; Atkinson, J.; Webb, M. Ice nucleation by particles immersed in supercooled cloud droplets. *Chem. Soc. Rev.* **2012**, *41*, 6519–6554. [[CrossRef](#)]

Disclaimer/Publisher's Note: The statements, opinions and data contained in all publications are solely those of the individual author(s) and contributor(s) and not of MDPI and/or the editor(s). MDPI and/or the editor(s) disclaim responsibility for any injury to people or property resulting from any ideas, methods, instructions or products referred to in the content.